Research Article | Vol. 31, No. 23 / 6 Nov 2023 / Optics Express 39039
Optics EXPRESS

Low-loss operation of silicon-on-insulator integrated components at 2.6–2.7 µm

HEIDI TUORILA,[1,*] JUKKA VIHERIÄLÄ,[1] MATTEO CHERCI,[2] MIKKO HARJANNE,[2] YISBEL MARIN,[2] SAMU-PEKKA OJANEN,[1] PENTTI KARIOJA,[3] AND MIRCEA GUINA[1]

[1]Optoelectronics Research Centre, Physics Unit, Tampere University, 33101 Tampere, Finland
[2]VTT Technical Research Centre of Finland, 02044 Espoo, Finland
[3]VTT Technical Research Centre of Finland, 90571 Oulu, Finland
[*]heidi.tuorila@tuni.fi

Abstract: Development of mid-infrared photonics is gaining attention, driven by a multitude of sensing applications requiring increasingly compact and cost-effective photonics systems. To this end, low-loss operation of µm-scale silicon-on-insulator photonic integration elements is demonstrated for the 2.6–2.7 µm wavelength region. The platform utilizes the 3 µm thick silicon core layer technology enabling demonstration of low-loss and low birefringence waveguides. Measurements of record low single mode waveguide propagation losses of 0.56 ± 0.09 dB/cm and bend losses <0.08 dB for various miniaturized bend geometries are presented and validated by simulation. Furthermore, a wavelength filter based on echelle grating that allows to select several operating channels within the 2.64–2.7 µm band, with a linewidth of ~1.56 nm for each channel is presented.

1. Introduction

Silicon photonic integrated circuits (PIC) enable the development of compact, reliable, and low-cost photonics-based systems for numerous applications. For example, integrated optical sensing solutions would find a wide variety of applications among biological, medical, environmental and industrial applications requiring lab-on-chip testing or advanced industrial process control [1].

Silicon photonics platforms have been widely developed for traditional telecommunication bands around 1.3 and 1.55 µm wavelengths but the mid infrared (MIR) range beyond 2 µm wavelength is less established yet has gained momentum [2,3]. For the conventional sub-micron silicon photonics, the wavelength range beyond 2.5 µm becomes challenging because in thin waveguides part of the field propagates in SiO_2 cladding that has an absorption peak at 2.6-2.9 µm [4,5]. Absorption is linked to H_2O band of vibrational transitions at 2.5-2.8 µm range. This has been shown to lead to high losses in the scale of 10-100 dB/cm [6]. Different approaches have been taken to mitigate this problem. Cheng et al. [7] used suspended membrane waveguides on SOI and demonstrated 3.0 dB/cm losses at 2.75 µm. Miller et al. [8] predicted using simulations that large core waveguides minimize the mode propagation in oxide cladding. There is also development outside SOI platform. Luke et al. [9] reported Si_3N_4 strip waveguides at 2.6 µm with 0.16 dB/cm losses. This Si_3N_4-platform uses SiO_2 cladding while Ge-on-Si allows SiO_2 free claddings and rib waveguides with approx. 3 dB/cm loss at 2.6-3.2 µm [10]. More recently, at 3.6-4.5 µm, Della Torre et al. [11] reported losses as low as 1.2-1.35 dB/cm for Ge-on-Si ridge waveguide. David et al. [12] on the other report Ge plasmonic waveguides at 5.6-11.2 µm with losses under 15 dB/mm. Recent research on Ge has concentrated on wavelengths above 3 µm

#497645 https://doi.org/10.1364/OE.497645
Journal © 2023 Received 16 Jun 2023; revised 29 Sep 2023; accepted 10 Oct 2023; published 2 Nov 2023

Optics EXPRESS

where two atmospheric windows [11] lie and also the two-photon absorption can be avoided [1,13].

In this paper we experimentally study μm-scale waveguide structures around 2.65 μm wavelength, which have been already demonstrated to exhibit very low losses at 1.3 μm [14] and 1.55 μm [15] bands. We demonstrate low losses down to 0.56 dB/cm. Moreover, we predict that the platform can maintain low losses up to 4 μm. Besides low losses, the large core waveguide allows low polarization dependency, good mode matching to III-V waveguides and single mode optical fibers and low power density that prevents undesired non-linear effects [15]. The use of large core waveguides combined with utilization of Euler bend design for small bending radius allows dense packaging [16]. Here we demonstrate extremely low bend losses below 0.08 dB achieved at around 2.65 μm. Besides addressing loss of waveguides, we demonstrate an echelle grating design that allows 1.56 nm spectral resolution around this wavelength band.

A specific problem we had to address is the need for developing waveguide testing solutions at mid-IR wavelengths. In this wavelength region, light sources, detectors, or single mode fibers each exhibit their own challenges in testing. In our testing approach we utilize wide spectral coverage supercontinuum lasers or narrow linewidth lasers.

2. Measurement setup

The setup used for broad-band transmission characterization is shown in Fig. 1. Depending on the specific band, addressed as a light source, it incorporated either supercontinuum (SC) laser sources or distributed feedback lasers (DFB-LD). In fact, we used two different SC sources (SC 1 and SC 2), both from Leukos, France, to produce a broadband emission. The specifications for all three sources are displayed in Table 1 including the estimations for the power coupled into a rib waveguide. Due to broadband emission from the SC-laser, the detection schemes in this case required wavelength discriminant detection sweeping over the spectrum. This was achieved either with a monochromator filtering the transmitted light before it reached a detector or with narrow band pass filters. High resolution, narrow bandwidth measurements, were carried out using two tunable DFB-LDs (DFB 1 and DFB 2). The key features of all light sources are listed in Table 1.

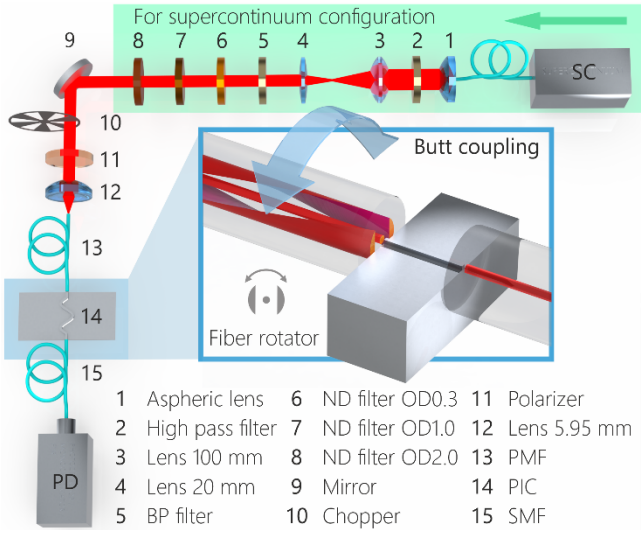

Fig. 1. Measurement setup configuration with the supercontinuum light source.

Optics EXPRESS

Table 1. Light source specifications

	SC 1	SC 2	DFB 1	DFB 2
Manufacturer	Leukos	Leukos	Nanoplus	Norcada
Total average output power	870 mW	350 mW	6.7 mW	> 6.0 mW
Wavelength bandwidth	1-3.5 µm	1-3.5 µm	1.4 nm at 2646 nm	4.4 nm at 2681 nm
Repetition rate	0.2 MHz	2 MHz	CW	CW
Pulse width	1.3 µs	200 ns	CW	CW
Power density in RIB	0.7 µW/nm	0.3 µW/nm	24 µw/nm	-
Peak power density in RIB	5.4 µW/nm	1.4 µW/nm	-	-
Peak power in RIB	3.2 mW	0.8 mW	0.03 mW	-

Components 1-5 in Fig. 1 were fixed in a lens tube that was connected to the SC output fiber. Lenses 3 and 4 act as a beam reducer to improve the coupling efficiency into fiber (13). To avoid destructive feedback to the source a tilted (7°) long pass filter (2) at 1.65 µm was used to remove the supercontinuum pump peak and the short wavelength tail of the SC-emission. A bandpass filter (5) at 2.4-3.0 µm was used to select the band of interest for the measurements. Neutral density filters OD 0.3-2.0 (6-8) were used to attenuate the optical power for various alignment and measurement purposes. For the DFB laser configuration, components 1-8 were not used. Instead, the light was collimated using a 5.95 mm diffraction limited aspheric lens. The mirror (9) with differential adjusters was used to align the beam. A chopper (10) enabled the use of a lock-in-amplifier to reduce the detection shot-noise by pulse excitation at 200 Hz. The 2 MHz pulse train from SC-laser is too high for the lock-in-amplifier used to reduce the high noise of the photodetector (PD) even when the detector (VIGO PVI-3 TE-3.4) with preamplifier (PIP-DC-20M-F-M4) was cooled down to 210 K. A high-power nanoparticle linear film polarizer (11) was used for selecting TE-polarization from unpolarized supercontinuum light and to enhance the extinction ratio of the TE-polarized DFB laser.

The polarization control in the setup is realized using a ZrF_4 polarization maintaining fiber (PMF) from Le Verre Fluoré. Due to the fragile nature and large bending radius of fibers made of ZrF_4, polarization control using stress-induced birefringence, typically employed at shorter wavelengths with more robust silica fibers, was not possible. In turn this leads to some specific design requirements for the set-up. We used a PMF (13) with a FC connector rotated, to match the TE-polarized beam arriving at the focusing lens (12) (5.95 mm diffraction limited aspheric). For the butt coupling into waveguide, the output of the PMF was stripped bare to reach visual access to the alignment between the fiber and the PIC channel to help with the initial alignment. The stripping itself was more complicated than normal due to the necessary use of hazardous chemicals. To control the polarization at the output end where light is launched into the PIC, we used a fiber rotator to control the alignment of fiber polarization axes. This arrangement is displayed in Fig. 1 (14). The fiber rotation was calibrated using a polarizer. The rotation causes some additional stress to the fiber, thus affecting the TE-mode confinement through changes in the refractive index. Because of this, the extinction ratio can be affected if the rotation to the fiber becomes too large. For these measurements the achieved extinction ratio was in the range of 13-19 dB. In addition, due to the fragility of the fiber large rotations were avoided.

The light was butt coupled into a waveguide from an as-cleaved fiber. The core of the PMF was 8.5 µm. The distance between the fiber and the PIC facet was on the scale of few microns estimated visually with a microscope. The output of the PIC channel was coupled similarly into an as-cleaved ZrF_4 single mode fiber (SMF) with a 9 µm core diameter. The fiber ends were initially visually positioned using a 3-axis nano-positioning piezo-controlled stages and the location trimmed by maximizing the coupled signal. The variation in the distance between

Optics EXPRESS

the fiber and the facet causes some variation in the measurement results, but the effect of this variation was assessed by repeated measurements with re-aligned fiber. The alignment error was estimated to cause a 0.3 dB variance in the output signal.

While the PIC waveguides used for the bend loss and echelle grating measurements were antireflection coated (ARC) to minimize possible feedback (the spiral waveguides for propagation loss measurement did not have an ARC), it was not possible to coat the cleaved fibers, thus resulting in a possible source of additional resonance caused by the reflections formed by sub-cavities like the reflecting fiber-ends. This introduced one additional source of uncertainty to the measurement, the effect of which was taken into account by observing the system through repeated measurements. It was observed that the minimized distance between the fiber and the PIC facet was prone to causing strong variations in the signal, assumed to be caused by a resonance between the fiber and the PIC facets. The effect was avoided by slightly increasing the distance between the fiber and the PIC which slightly reduced the coupling efficiency but allowed for more stable and repeatable signal level.

3. Characterization

3.1. Simulations

For 3 µm thick SOI waveguides, under study in this work, the optical field is more confined in the core than in the case of typical sub-micron scale waveguides. Figure 2(b) and (d) display the mode field confinement at 2650 nm for both standard 220 nm x 480 nm and the 3 µm x 1.875 µm strip waveguides to illustrate the improvement in mode confinement respect to the sub-micron structure. For comparison, similar schematics are provided in Fig. 2(a) and (c) for the 1550 nm wavelength to highlight the importance of good mode confinement in mid-IR region. The 3 µm strip waveguide profile corresponds to a multimode waveguide and the simulations in Fig. 2 only display the fundamental TE mode. In practice, the 3 µm strip waveguides are used together with single-mode 3 µm rib waveguides. By combining the strip geometry with the Euler bend design, the excitation of the higher order modes can be suppressed or minimized. The simulations were made using FIMMWAVE [17] software with the real finite-difference method (FDM) solver and boundary conditions set to electric/magnetic as they are suited for calculations of guided modes in structures without bends or optical leakage.

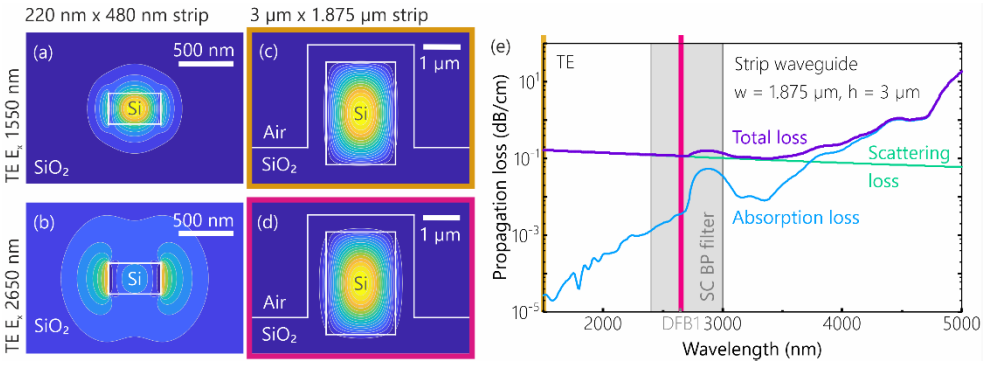

Fig. 2. Mode field confinement for strip waveguides: a) submicron waveguide at 1550 nm, b) submicron waveguide at 2650 nm, c) 3 µm waveguide at 1550 nm and d) 3 µm waveguide at 2650 nm. e) Simulation for propagation losses in 3 µm x 1.875 µm strip waveguide including both scattering and absorption losses with material loss data from Ref. [18].

This better confinement translates into an ultra-wide wavelength range of operation for thick SOI waveguides, from 1.2 µm up to 4 µm, and possibly beyond, if the geometry is optimized

Optics EXPRESS

and the SiO_2 cladding is removed. The total propagation losses (α_{total}) in the near-infrared and short-wavelength infrared are dominated by radiation losses (α_{rad}) due to the coupling of the guided mode into radiation modes. This is caused by the effective index (n_{eff}) variations induced by the sidewall roughness, which basically introduce a waveguide width variation. However, in the mid-infrared, the cladding absorption (α_{abs}) begins to be quite detrimental for wavelengths greater than 3.5 μm [18]. Thus, the total losses in the supported wavelength range are given by $\alpha_{total} = \alpha_{rad} + \alpha_{abs}$.

The radiative losses are defined by the Lacey-Payne model as [19]:

$$\alpha_{rad}=\varphi^2\left(\frac{w}{2}\right)(n_{core}^2 - n_{clad}^2)\frac{{k_0}^3}{4\pi n_{core}}\int_0^{\pi}\tilde{R}(\beta n_{clad}k_0\cos\theta)d\theta, \quad (1)$$

where $\varphi(w/2)$ is the mode field at the waveguide surface, which depends only on the waveguide geometry and material composition, w is the waveguide width, n_{core} and n_{clad} are the refractive index of the core and cladding respectively and $k_0 = 2\pi/\lambda$ is the wavenumber in free space. The spectral density function of the sidewall roughness, $\tilde{R}(\Omega)$, is a function of the roughness spatial frequencies $\Omega = \beta - n_{clad}k_0\cos\theta$, with β as the propagation constant of the mode and θ as the scattering angle in respect to the waveguide axis. This function is related to the autocorrelation function of surface roughness, which typically follows exponential statistics for waveguides such as the ones considered here and depends on the correlation length L_c and the standard deviation σ of the roughness. This model was originally formulated for slab waveguides but was later extended to 2D waveguides by employing the effective index method [20]. To obtain the 1D waveguide corresponding to our 3 μm thick and 1.875 μm wide strip, we calculated the effective index of a 3 μm thick Si slab waveguide with top and bottom SiO_2 claddings using FIMMWAVE [17]. Thus, we obtained the refractive index of the core of a 1.875 μm wide equivalent waveguide. Finally, we assumed that the roughness was characterized by $\sigma = 2$ nm and $L_c = 50$ nm, which are typical values for waveguides that have gone through roughness smoothing using thermal oxidation [21], like it is in our case.

The loss induced by the cladding absorption is given by $\alpha_{abs} = 4\pi\mathrm{Im}(n_{eff})/\lambda$. We calculated the effective index of the strip waveguide using the complex finite-difference method (FDM) solver from FIMMWAVE [17], specifying the wavelength dependent material attenuation in 1/cm, obtained from the data provided in [18]. In reality, the optical properties of SiO_2 are highly dependent on the precursor and deposition method (tetraethyl orthosilicate (TEOS) with Low Pressure Vapor Deposition (LPCVD) for our waveguides), but there is no available data for the wavelength range under consideration.

The estimated total loss is shown in Fig. 2(e). The results show that the contribution from scattering losses decreases with increasing wavelength, which is hinted by the ${k_0}^3$ factor in Eq. (1), and there is good agreement with the measured losses around 1550 nm (~0.15 dB/cm) [15]. For wavelengths below ~2.6 μm the losses are dominated by radiation losses, whereas for longer wavelengths the contribution from the cladding absorption begins to be significant, as predicted before. It is important to highlight the absorption band stretching from 2.63 μm to 3.45 μm due to the presence of the OH groups in the SiO_2 structure [22]. This band covers the wavelength of interest and can be detrimental for the performance of devices operating in this range.

3.2. Propagation losses

For propagation loss measurements we used a spiral with 1.875 μm wide waveguides of four different lengths: 1.7, 8.30, 14.90 and 21.50 cm. The use of different length allowed to extrapolate the propagation loss independent on the coupling losses. Light from DFB 1 LD at 2646 nm was butt coupled in and out of waveguides and measured using the photodiode. There was no antireflection coating on the facet at the measurement wavelength, causing Fabry-Perot resonance

Optics EXPRESS

for the signal passing the waveguide cavity. As the cavity of the spiral is quite long, the resonance has a small period leading to the noise-like appearance of the measured curve. Measurements with shorter cavities (5 mm) showed tidy, even Fabry-Perot oscillation, confirming the source of the effect. Other sources, such as the presence of the higher order modes (HOM) causing the oscillation is unlikely as the Euler bends used in the spiral have a high HOM extinction ratio. Thus, the entire current tuning range of the DFB laser was scanned and the voltage - current (V-I) characteristics of a single measurement were fitted with the average slopes (Fig. 3(a)) and then compared with the reference channel for each waveguide length to circumvent the signal oscillation. The results are displayed in Fig. 3(b). After a linear fit of the resulting values, we reached the propagation loss of 0.56 ± 0.09 dB/cm. While no extensive repeat measurements were made in this case the fact, that the normalized loss values in Fig. 3(b) are well compatible with the linear fit giving confidence on the viability of the method. The error estimate of 0.09 dB/cm was made by analyzing the possible variations in the linear fits of the I-V characteristics. The dip in the measured curves around 120 mA is caused by the H_2O absorption and is also visible in the signal measured directly from the DFB laser.

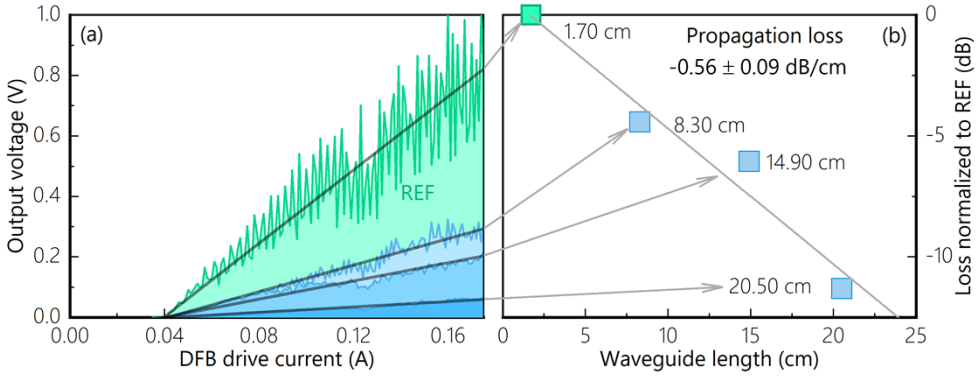

Fig. 3. Waveguide propagation loss measurement using different lengths of spiral waveguides. a) Drive current - output power curves for each spiral waveguide. The effect of the Fabry-Perot resonance is circumvented through an averaged linear fit. b) The slope of each linear fit was used to calculate the respective data points for the propagation loss.

3.3. Bend losses

Six different bend geometries displayed Fig. 4(a) and their losses were characterized. The bends were measured using the SC 2 source. To estimate the loss value per bend, multiple bends were serialized to increase the total loss. For reference, to remove the fiber to waveguide coupling loss, a transmission from a 3 µm wide rib waveguide was measured and the transmission from each bend waveguide referenced to this. The waveguide specifications and measured losses per bend are listed in Table 2.

3.4. Echelle grating

The echelle grating filter design is illustrated in Fig. 4(c). The filter is based on a concept where the input signal is directed to a circular grating that simultaneously diffracts the light and focuses each band in their respective output channels. The input and output channels and the grating are placed on the circumference of the so-called Rowland circle while the grating arc radius is twice the radius of the Rowland circle (R) [23]. The input and output channel locations are calculated from the target absorption wavelengths and the selected grating period. The following specifications were used for the filter: grating period 8.0 µm, grating order 19, R = 2600 µm,

Optics EXPRESS

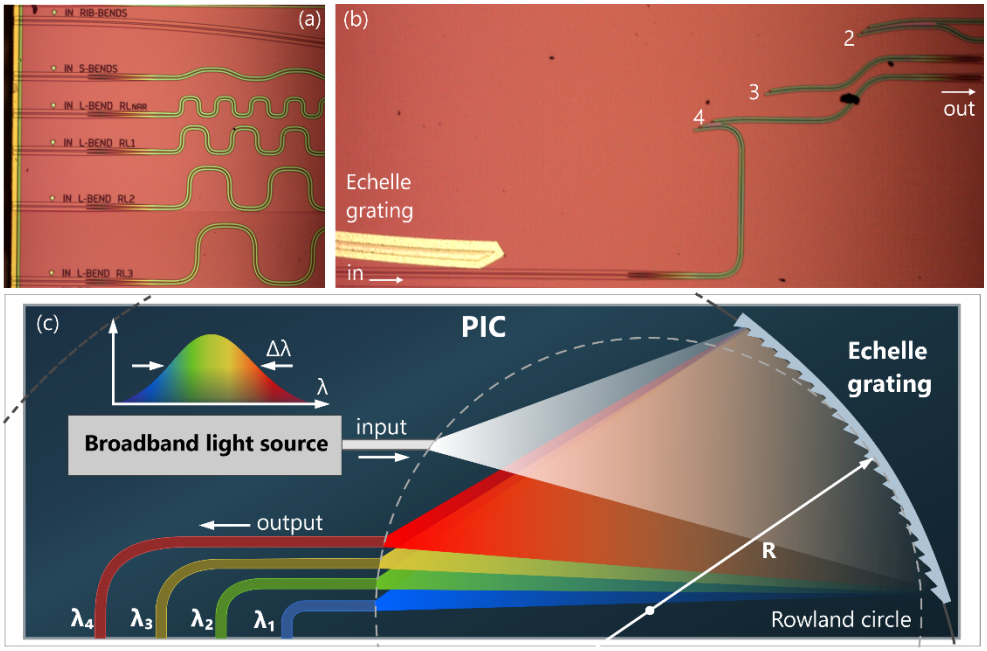

Fig. 4. Microscope images of the SOI platform. a) Bend waveguides with tapers at in and output. b) Echelle grating filter with four output channels. c) Echelle grating filter concept figure.

Table 2. Bend waveguide characteristics

Waveguide type	Number of bends	Width (μm)	Minimum bending radius	Loss / bend (dB)
Rib S-bend	3	3	5 mm	0.06 ± 0.12
Strip S-bend	34	1.875	72.75 μm	0.021 ± 0.008
Strip L-bend	174	1.5	12.5 μm	0.08 ± 0.08
Strip L-bend	120	1.875	18.0 μm	0.015 ± 0.003
Strip L-bend	72	1.875	29.0 μm	0.013 ± 0.005
Strip L-bend	52	1.875	41.5 μm	0.014 ± 0.009

input/output waveguide angles 140°/130°, and waveguide width 3.0 μm. The designed echelle filter was simulated using EPIPPROP software v 1.3 from Photon Design; the calculated spectrum is shown in Fig. 5(a). The reflector was fabricated by etching the grating pattern through the SOI. A layer of oxide followed by an aluminum coating were then deposited on the SOI sidewall. The fabricated device is shown in Fig. 4(b).

We designed and fabricated an echelle filter with four output channels initially chosen to target absorption peaks of CH_4 at 2647.5 nm, H_2S at 2650 nm and 2699.6 nm, and CO_2 at 2682 nm that we measured using a monochromator. For this measurement the SC 1 source was used to provide an adequately wide source spectrum. Each output channel was butt coupled into SM fiber that was connected to the monochromator. The measured spectra with their peak wavelengths are displayed in Fig. 5. For channels 1 and 2 (Fig. 5(b)) TE polarized and light was used. For the channel 1 the TE peak is split in two by water absorption peak that can be seen in the reference measurement from rib waveguide displayed in the same figure. These atmospheric spectral fingerprints along with the DFB 1 laser were also used to calibrate the monochromator. For the channels 3 and 4 in Fig. 5(c) only unpolarized signal could be detected due to polarizer

Optics EXPRESS

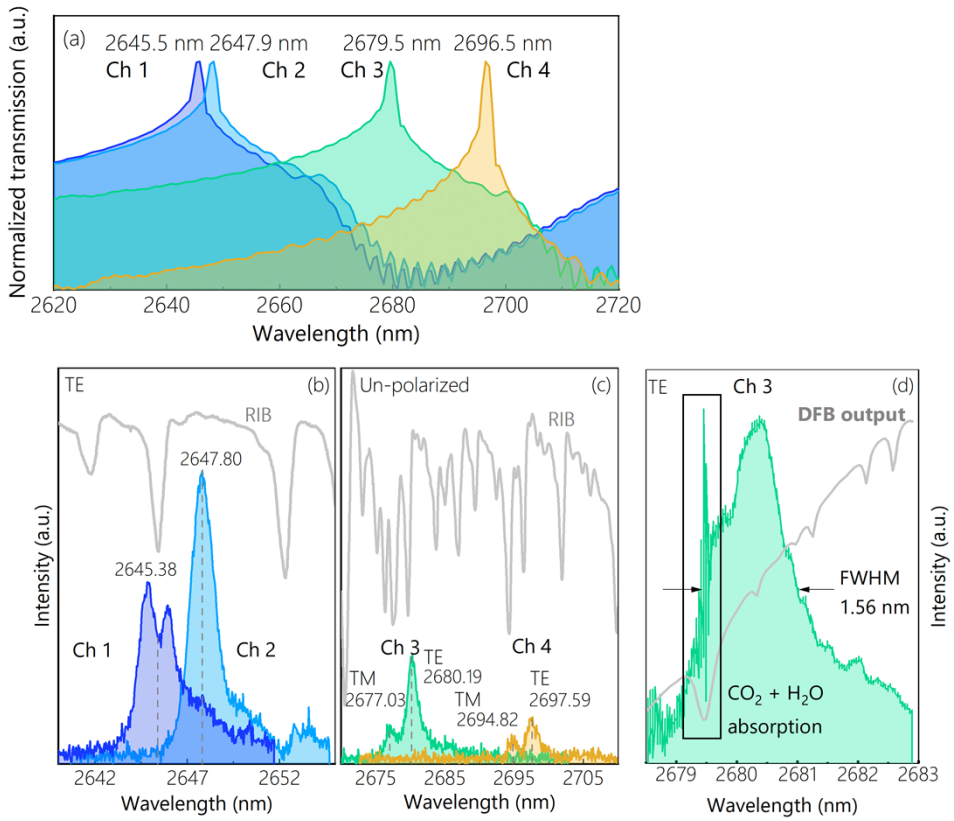

Fig. 5. a) Simulated echelle filter peaks. b) Echelle filter spectrum for channels 1 and 2 using supercontinuum light source and monochromator with TE polarized light. Water absorption peak splits the ch 1 peak. c) Spectrum from channels 3 and 4 with unpolarized light. d) Channel 3 measured with DFB laser (TE polarized light) for linewidth analysis. FWHM of the peak is 1.56 nm. The DFB 2 LD output is displayed in gray.

dampening the weak signal. Comparison with the simulated results in Fig. 5(a) show a good agreement with the measured peak locations.

The resolution of the monochromator measurement varied across the measured spectra due to the differences in available signal strengths. The rib measurement had the highest resolution followed by the channels 1 and 2 and finally the channels 3 and 4 exhibiting the poorest resolution due to the weak signal. Because of this, the peak details are not directly comparable, and the focus of the measurement was on the location of the peaks. The signal weakness in the channels 2 and 3 is likely caused by the atmospheric absorption by the species such as H_2O or CO_2 as in this area the presence of these absorption spectra is strong. The increase in absorption is visible by the comparing of the rib spectra in Fig. 5(b) and (c) where there is significant increase in disturbance in Fig. 5(c). While the monochromator resolution was set at the highest possible value, it is still likely not displaying the rib spectrum absorption in full detail and it is likely that the absorption could be even stronger in this area than conveyed by the rib spectrum. Thus, it was concluded that the poor signal from channels 3 and 4 is a result of the room air, free space test setup. For improved measurements it would be necessary to build a climate controlled, closed system. From the unpolarized signal an additional TM peak can be seen in the spectra. This shift between TE and TM-polarization states, characteristic to diffraction grating filters, is caused by

Optics EXPRESS

the birefringence of the echelle slab. The shift of the TM-polarization peak is approximately 2.9 nm.

The monochromator had too poor resolution to resolve the filtered peaks in detail. To estimate the linewidth, we measured the channel. 3 using the DFB 2 LD that has a tuning range coinciding with the peak. The spectrum is displayed in Fig. 5(d). The upper limit for the full width half maximum (FWHM) was estimated to be 1.56 nm. The noise peak in the spectrum is caused by the coincident H_2O and CO_2 absorption peaks. This can be also seen from the dip in the DFB output power.

4. Conclusions

A characterization set-up and experimental procedure use for estimating waveguide losses in µm-scale SOI technology platform for operation at 2-3 µm range was introduced. The results prove the low loss performance of waveguides; propagation losses as low as 0.56 dB/cm, bend losses of 0.015 dB/cm per bend for 18 µm minimum bending radius were demonstrated. Moreover, we demonstrate high resolution wavelength discrimination based on an echelle grating filter allowing resolutions down to 1.56 nm around 2.6-2.7 µm wavelength. These elements constitute key building blocks allowing migration of SOI-based integrated photonics circuits towards mid-IR spectral region, of high interest for spectroscopic and sensing applications. Besides understanding the performance of the building blocks reported here, the testing methods have recently allowed us to characterize more complex circuits [24].

Funding. H2020 Industrial Leadership (644192); Business Finland (44761); Business Finland (1613); Academy of Finland (320168); Tekniikan Edistämissäätiö (7736).

Acknowledgements. The work is a part of the Academy of Finland Flagship Programme PREIN #320168. H. Tuorila thanks Finnish Foundation for Technology Promotion for the provided support in funding.

Disclosures. The authors declare no conflicts of interest.

Data availability. The data related to the results presented in this paper is not currently publicly available but may be obtained from the authors upon reasonable request.

References

1. R. Soref, "Mid-infrared photonics in silicon and germanium," Nat. Photonics **4**(8), 495–497 (2010).
2. J. M. Fedeli and S. Nicoletti, "Mid-Infrared (Mid-IR) Silicon-Based Photonics," Proc. IEEE **106**(12), 2302–2312 (2018).
3. H. Lin, Z. Luo, T. Gu, L. C. Kimerling, K. Wada, A. Agarwal, and J. Hu, "Mid-infrared integrated photonics on silicon: a perspective," Nanophotonics **7**(2), 393–420 (2017).
4. A. Schliesser, N. Picqué, and T. W. Hänsch, "Mid-infrared frequency combs," Nat. Photonics **6**(7), 440–449 (2012).
5. I. E. Gordon, L. S. Rothman, C. Hill, *et al.*, "The HITRAN2016 molecular spectroscopic database," J. Quant. Spectrosc. Radiat. Transfer **203**, 3–69 (2017).
6. R. A. Soref, S. J. Emelett, and W. R. Buchwald, "Silicon waveguided components for the long-wave infrared region," J. Opt. A: Pure Appl. Opt. **8**(10), 840–848 (2006).
7. Z. Cheng, X. Chen, C. Y. Wong, K. Xu, and H. K. Tsang, "Mid-infrared Suspended Membrane Waveguide and Ring Resonator on Silicon-on-Insulator," IEEE Photonics J. **4**(5), 1510–1519 (2012).
8. S. A. Miller, M. Yu, X. Ji, A. G. Griffith, J. Cardenas, A. L. Gaeta, and M. Lipson, "Low-loss silicon platform for broadband mid-infrared photonics," Optica **4**(7), 707 (2017).
9. K. Luke, Y. Okawachi, M. R. E. Lamont, A. L. Gaeta, and M. Lipson, "Broadband mid-infrared frequency comb generation in a Si3N4 microresonator," in *Conference on Lasers and Electro-Optics Europe - Technical Digest* (Institute of Electrical and Electronics Engineers Inc., 2015), Vol. 2015-Augus, pp. 4823–4826.
10. L. Shen, N. Healy, C. J. Mitchell, J. S. Penades, M. Nedeljkovic, G. Z. Mashanovich, and A. C. Peacock, "Mid-infrared all-optical modulation in low-loss germanium-on-silicon waveguides," Opt. Lett. **40**(2), 268 (2015).
11. A. Della Torre, M. Sinobad, R. Armand, B. Luther-Davies, P. Ma, S. Madden, A. Mitchell, D. J. Moss, J.-M. Hartmann, V. Reboud, J.-M. Fedeli, C. Monat, and C. Grillet, "Mid-infrared supercontinuum generation in a low-loss germanium-on-silicon waveguide," APL Photonics **6**(1), 016102 (2021).
12. M. David, A. Dabrowska, M. Sistani, I. C. Doganlar, E. Hinkelmann, H. Detz, W. M. Weber, B. Lendl, G. Strasser, and B. Hinkov, "Octave-spanning low-loss mid-IR waveguides based on semiconductor-loaded plasmonics," Opt. Express **29**(26), 43567–43579 (2021).
13. N. K. Hon, R. Soref, and B. Jalali, "The third-order nonlinear optical coefficients of Si, Ge, and Si 1-xGex in the midwave and longwave infrared," J. Appl. Phys. **110**(1), 011301 (2011).

Optics EXPRESS

14. T. Aalto, M. Harjanne, B.-J. Offrein, C. Caër, C. Neumeyr, A. Malacarne, M. Guina, R. N. Sheehan, F. H. Peters, and P. Melanen, "Integrating III-V, Si, and polymer waveguides for optical interconnects: RAPIDO," in *Optical Interconnects XVI*, H. Schröder and R. T. Chen, eds. (SPIE, 2016), Vol. 9753, p. 97530D.
15. T. Aalto, M. Cherchi, M. Harjanne, S. Bhat, P. Heimala, F. Sun, M. Kapulainen, T. Hassinen, and T. Vehmas, "Open-Access 3-µm SOI Waveguide Platform for Dense Photonic Integrated Circuits," IEEE J. Select. Topics Quantum Electron. **25**(5), 1–9 (2019).
16. M. Cherchi, S. Ylinen, M. Harjanne, M. Kapulainen, and T. Aalto, "Dramatic size reduction of waveguide bends on a micron-scale silicon photonic platform," Opt. Express **21**(15), 17814 (2013).
17. FIMMWAVE, "Photon Design - Your source of photonics CAD tools," https://www.photond.com/.
18. R. Kitamura, L. Pilon, and M. Jonasz, "Optical constants of silica glass from extreme ultraviolet to far infrared at near room temperature," Appl. Opt. **46**(33), 8118–8133 (2007).
19. F. P. Payne and J. P. R. Lacey, "A theoretical analysis of scattering loss from planar optical waveguides," Opt. Quantum Electron. **26**(10), 977–986 (1994).
20. K. K. Lee, D. R. Lim, H. C. Luan, A. Agarwal, J. Foresi, and L. C. Kimerling, "Effect of size and roughness on light transmission in a Si/SiO2 waveguide: Experiments and model," Appl. Phys. Lett. **77**(11), 1617–1619 (2000).
21. K. K. Lee, D. R. Lim, L. C. Kimerling, J. Shin, and F. Cerrina, "Fabrication of ultralow-loss Si/SiO2 waveguides by roughness reduction," Opt. Lett. **26**(23), 1888 (2001).
22. A. Goullet, C. Vallée, A. Granier, and G. Turban, "Optical spectroscopic analyses of OH incorporation into SiO2 films deposited from O2/tetraethoxysilane plasmas," J. Vac. Sci. Technol., A **18**(5), 2452–2458 (2000).
23. J. Brouckaert, W. Bogaerts, P. Dumon, D. Van Thourhout, and R. Baets, "Planar Concave Grating Demultiplexer Fabricated on a Nanophotonic Silicon-on-Insulator Platform," J. Lightwave Technol. **25**(5), 1269–1275 (2007).
24. S. P. Ojanen, J. Viheriälä, M. Cherchi, N. Zia, E. Koivusalo, P. Karioja, and M. Guina, "GaSb diode lasers tunable around 2.6 µ m using silicon photonics resonators or external diffractive gratings," Appl. Phys. Lett. **116**(8), 081105 (2020).